

Mechanical properties of tape cast nickel-based anode materials for solid oxide fuel cells before and after reduction in hydrogen

M. Radovic, E. Lara-Curzio *

Metals and Ceramics, Oak Ridge National Laboratory, 1 Bethel Valley Road, Oak Ridge, TN 3783 16069, USA

Received 16 August 2004; accepted 20 August 2004

Abstract

The processing of solid oxide fuel cells (SOFCs) often involves co-sintering of multi-layered stacks. In the case of SOFCs incorporating Ni-based anodes, hydrogen reduction of the anode usually takes place during the first service cycle of operation or conditioning. Initial reduction causes changes in the chemistry, microstructure and properties of the Ni-based anode material, which in turn induce mechanical stresses in the cell. In this study the elastic moduli, biaxial strength and fracture toughness of unreduced (NiO-YSZ) and reduced (Ni-YSZ) anode were determined as functions of porosity. Elastic properties were determined by impulse excitation at ambient temperature. Biaxial strength and fracture toughness were determined at ambient temperature by the ring-on-ring and double torsion test methods, respectively. It was found that the mechanical properties of unreduced and reduced Ni-based anode materials depend strongly on porosity. Property–porosity trends were found to be in good agreement with prediction of the minimum solid area model. Results presented in this study show that the elastic moduli and biaxial strength of the Ni-based anode material decreases after reduction in hydrogen while fracture toughness increases after reduction due to formation of ductile Ni-metal phase.

Published by Elsevier Ltd on behalf of Acta Materialia Inc.

Keywords: SOFC; Toughness; Elastic behavior; Fracture; Hydrogen

1. Introduction

Solid oxide fuel cells (SOFC) are electrochemical devices that transform the chemical energy of fuel (hydrogen natural gas, etc.) directly to electrical energy. As highly efficient and pollution-free energy sources SOFCs have been intensively studied during the past decade [1,2]. Although the reliability of SOFCs depends not only on the chemical and electrochemical stability of its components but also on the capability of the SOFC components to withstand mechanical stresses that arise during processing and service, limited work has been re-

ported on the mechanical properties of the SOFC's components.

A typical SOFC consists of a multi-layered stack of cells comprised of a fully dense electrolyte layer capable of conducting oxygen ions, and electrically conducting, porous anode and cathode layers, and interconnectors. At present, a cermet consisting of Ni-metal and Y_2O_3 -stabilized ZrO_2 is widely used as an anode material in high temperature SOFCs [1–3]. This material is preferred because of its good electronic conductivity, chemical and structural stability, catalytic properties and compatibility with other materials in SOFCs [1]. The porosity of Ni-based anodes (up to 50 vol%) makes it possible to achieve high external current densities while keeping internal current densities and over potentials low. It also enables hydrogen to diffuse through the cermet and H_2O to escape from it [4]. While Ni metal has a

* Corresponding author. Tel.: +1 86 5574 0034; fax: +1 86 5574 6098.

E-mail address: radovicm@ornl.gov (M. Radovic).

vital role as a catalyst for electrochemical reactions on the anode side of the SOFC and as an electrical conductor [3], the role of YSZ is mainly to support Ni particles and prevent them from sintering during service. Also, YSZ is used to match the thermal expansion of the anode close to that of the YSZ electrolyte. In most cases porous Ni-based anodes are fabricated starting with precursors consisting of NiO and YSZ (NiO-YSZ), and then co-sintered with the electrolyte and cathode. When hydrogen fuel is supplied to the cell for the first time, NiO-YSZ is converted into a Ni-YSZ cermet. As a result of NiO reduction into Ni-metal the volume and porosity of the anode layer change, as well as its physical and mechanical properties. The initial reduction process introduces mismatch stresses in multi-layered SOFC components, which in turn could have an effect on the reliability and structural integrity of SOFCs [5].

The decrease of Young's and shear moduli of NiO-YSZ with porosity have been reported earlier by Selcuk and Atkinson [6,7] and Radovic et al. [8,9]. It was shown that Young's modulus of NiO-YSZ decreases almost by half from ≈ 200 GPa to ≈ 110 GPa with increase in porosity from 0 to 23 vol%. More recently, Radovic and Lara-Curzio [9] showed that Young's and shear moduli of Ni-based anode with initial porosity of 23 vol% decrease approximately by 45% after hydrogen reduction mainly due to increase in porosity. The Young's modulus of ≈ 60 GPa determined for fully reduced Ni-based anodes is considerably lower than that of the adjacent YSZ electrolyte layer (≈ 200 GPa [11]) which, in turn, has a significant effect on the stress redistribution in the multi-layered SOFC [5].

The reduction of Ni-based anode materials also results in microstructural changes that could determine the type, size and distribution of strength controlling defects. Components of planar SOFC stacks are mainly exposed to biaxial states of stress that result from the thermal expansion mismatch between the cell constituents and temperature gradients during the operation. Thus, it has been customary to determine the in-plane biaxial strength of SOFC materials using the concentric ring-on-ring flexural-loading configuration. Atkinson and Selcuk [7] determined the ambient temperature biaxial strength of 187 MPa and Weibull modulus of 11.8 for 75 mol% NiO-YSZ samples of unknown porosity, while Radovic et al. [8] reported on decrease in the room temperature biaxial strength of NiO-YSZ with increasing porosity.

The main goal of this work is to study the effect of porosity and hydrogen reduction on the room temperature elastic properties, fracture toughness and biaxial strength of Ni-based SOFC anode with 75 mol% NiO. Elastic moduli of the unreduced and reduced Ni-based anode material were determined by impulse excitation. In-plane biaxial strength was determined using the ring-on-ring configuration, while fracture toughness

was obtained from the double torsion tests. The microstructural changes that occur during hydrogen reduction were also studied and related to observed changes in mechanical properties.

2. Experimental procedure

The Ni-based anode material examined in this study was prepared from a powder mixture of NiO (J.T. Baker, ¹ Phillipsburg, NJ) and ZrO₂ stabilized with 8 mol% Y₂O₃, YSZ (TOSOH Corp. ¹, Grove City, OH). The powder mixture contained 75 mol% of NiO. Different amounts of organic pore former (rice starch, ICN Biomedicals ¹, Inc, Irvine, CA) were added to the powder mixture to obtain samples with different levels of porosity. Green samples were prepared by tape casting ≈ 250 μ m thick single layers. Two, four or six green tapes were subsequently laminated to make samples of different thickness. Discs for determination of elastic properties and in-plane biaxial strength with nominal diameter of 25.4 mm were hot-knifed from the laminated green tapes and sintered at 1400 °C in air for 2 h. Rectangular samples for double torsion testing were cut from tapes previously sintered also at 1400 °C in air for 2 h. Approximately one half of the samples were reduced in 4% H₂ and 96% Ar gas mixture at 1000 °C for 30 min. The relative porosity of each sample before and after reduction was determined using the standard alcohol immersion method [10].

The elastic properties of un-reduced and reduced anode samples, namely Young's and shear moduli were determined by impulse excitation (IE) [9] using the commercially available Buzz-o-sonic ¹ software program (BuzzMac Software, Glendale, WI). Disc-shaped specimens supported by a foam material on its nodal lines were excited by a light mechanical impulse [9]. A microphone, located in the vicinity of the sample is used to transmit sound vibrations to the signal-processing unit. The fundamental resonance frequencies, in both torsional and flexural mode were identified, which in turn can be used to calculate values of Young's and Shear moduli [11] using the following equation:

$$E_{1,2} = \frac{37.6991 f_{1,2}^2 D^2 m (1 - \nu)}{K_{1,2}^2 t^3}, \quad (1)$$

where D , m , and t are diameter, mass and thickness of the sample, respectively. $E_{1,2}$ are Young's moduli calculated from the first (f_1) and second (f_2) natural resonant

¹ Certain commercial equipment, instruments, or materials are identified in this paper in order to specify the experimental procedure adequately. Such identification is not intended to imply recommendation or endorsement by Oak Ridge National Laboratory, nor is it intended to imply that the materials or equipment identified are necessarily the best available for the purpose.

frequencies. Poisson's ratio, ν was determined according to ASTM C1259 as a function of $2t/D$ and f_2/f_1 , as well as the first and second natural geometric factors, $K_{1,2}$. Shear modulus, G , was determined according to the following equation:

$$G = E/[2(1 - \nu)]. \quad (2)$$

Concentric ring-on-ring configuration [12–14] was used to determine in-plane biaxial strength of Ni-based anode at room temperature. In this configuration the disk-shaped test specimens with diameter (D) of ≈ 25 mm were spaced concentrically between a loading ring with diameter (D_l) of 5.5 mm and a supporting ring with diameter (D_s) of 20 mm. The loading and unloading rings were machined from Delrin (supplier McMaster-Carr¹, GA). Load was applied to the samples at a constant cross-head displacement rate of 1 mm/min and equibiaxial strength was calculated using the following equation:

$$\sigma_f = \frac{3 \cdot F}{2\pi h^2} \left[(1 - \nu) \frac{D_s^2 - D_l^2}{2D^2} + (1 + \nu) \ln \frac{D_s}{D_l} \right], \quad (3)$$

where F , h and ν are braking load, sample thickness and Poisson's ratio, respectively. Eq. (3) was derived using small-displacements elastic theory assuming that the sample exhibits linear-elastic behavior throughout the test. In order to obtain an error of only $\sim 2\%$, finite element analyses show [14] that displacement has to be within $h/4$, i.e. the following criterion has to be satisfied [12]:

$$h \geq \sqrt{2\sigma_f D_s^2 / 3E}, \quad (4)$$

where E is Young's modulus. The criterion expressed by Eq. (4) was satisfied for all samples examined in this study except in the case of some bi-layered samples that failed at the highest stresses. Even in those cases the maximum deflection of the samples was well below $h/2$, which resulted in an error smaller than 6% [14]. In all characterized samples failure originated within perimeter of the loading ring and was in agreement with guidance provided by ASTM test method C1499 [12].

The fracture toughness, K_{IC} , of Ni-based anode material was determined by double torsion testing [15–17] using rectangular samples (20 mm in width, S , 40 mm in length, L , and ≈ 1 mm thick, t). Initial notches 1 mm wide and 12.5 mm long were introduced into one side of the sample using a circular diamond blade. The notch tip was machined such that the thickness of the specimen at the notch tip tapered from very thin to the full thickness. This facilitates the formation of a sharp precrack at the notch tip at relatively low loads. All notched test specimen were precracked by loading the sample at a rate of 0.02 mm/min. For valid fracture toughness measurements, it is necessary to ensure that the cumulative length of notch and precrack is in the

constant K_I range, which is described as $0.55S < (\text{notch length} + \text{precrack length}) < L - 0.65S$ [16]. This condition was satisfied for all tests reported in this paper. Precracked samples were loaded at loading rate of 2 mm/min to cause fast fracture. The fracture toughness of Ni-based anode samples was calculated using the following equation:

$$K_{IC} = PS_m \left[\frac{3(1 + \nu)}{St^4 \xi} \right]^{1/2}, \quad (5)$$

for the plain stress conditions where S_m is the moment arm, S specimen width, t the plate thickness, ν Poisson's ratio, P critical load (onset of fast fracture) and ξ thickness correction factor given as: $\xi = 1 - 1.26(t/S) + 2.4(t/S) \exp(-2\pi S/2t)$ [16].

The microstructure and fracture surfaces of unreduced and reduced Ni-based anode samples with different porosity were analyzed using a field emission scanning electron microscope (FESEM) Hitachi S4700¹.

3. Experimental results and discussion

3.1. Structural changes during reduction

In addition to changes in the chemical composition of Ni-based anode materials during reduction, the porosity of the anode samples changes as well. This is expected since the specific volume of metallic Ni is significantly smaller than that of NiO. FESEM analysis revealed that the pores that formed due to shrinkage of NiO particles during reduction are much smaller (1–2 μm) than those initially present in NiO-YSZ samples (≈ 10 μm). The increase in porosity as a result of hydrogen reduction is clearly demonstrated in Fig. 1 where relative porosity

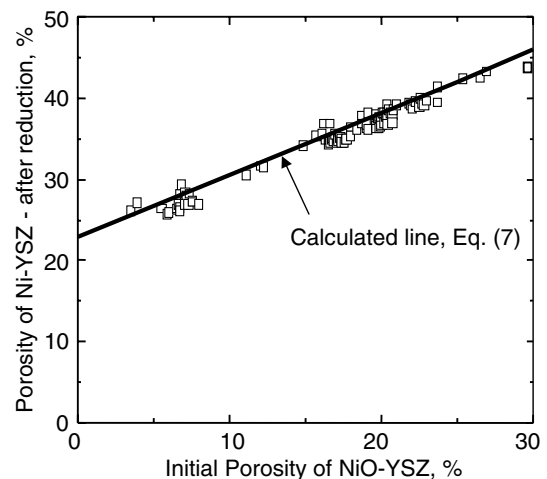


Fig. 1. Relationship between relative porosity of the reduced anode samples and initial porosity of the samples before reduction. Open square symbols represent experimental results determined by alcohol immersion method, while the solid line corresponds to Eq. (7).

of the reduced anode is plotted versus initial porosity of the samples. The open square symbols in Fig. 1 represent results obtained experimentally by the alcohol immersion method.

If we assume that the decrease of the overall volume of anode samples after reduction is negligible, then the following expression can be derived for the porosity of the anode sample after reduction, p , as a function of initial porosity before reduction, p_0 :

$$p = p_0 + (1 - p_0) \cdot \bar{m}_{\text{NiO}}^0 \cdot \left[\frac{1}{\rho_{\text{NiO}}} - \frac{1}{\rho_{\text{Ni}}} + \frac{m_0}{m_{\text{NiO}}} \cdot \frac{1}{\rho_{\text{Ni}}} \right], \quad (6)$$

where ρ_{Ni} and ρ_{NiO} are the density of Ni and density of NiO, respectively. \bar{m}_{NiO}^0 is the initial weight fraction of NiO in the NiO-YSZ composite. For the examined NiO-YSZ composite the initial weight fraction of NiO was $\bar{m}_{\text{NiO}}^0 = 0.587$. For $\rho_{\text{Ni}} = 8.88 \text{ g/cm}^3$ and $\rho_{\text{NiO}} = 6.67 \text{ g/cm}^3$ Eq. (6) yields:

$$p = 0.228 + 0.772p_0. \quad (7)$$

Eq. (7) has also been plotted in Fig. 1 as a solid line confirming the good agreement with the experimental results.

The most prominent structural changes that occur as a result of hydrogen reduction take place in areas where NiO particles form clusters/agglomerates like the one shown in Fig. 2(a). NiO clusters form a coarse, foamy Ni-metal structure after reduction as illustrated in Fig. 2(b). Clusters of NiO and Ni-metal particles/grains were observed in all examined samples and in most cases neither zirconium nor yttrium were detected within those clusters by EDS.

3.2. Elastic properties

A large number of empirical and theoretical models have been proposed to express the dependence of the magnitude of Young's and Shear moduli on the volume

fraction of porosity. In the present work, the following two expressions describing elastic moduli as a function of porosity were fitted to the experimental modulus–porosity data

$$M = M_{\text{fd}} \exp(-b_M p'), \quad (8)$$

$$M = M_{\text{fd}} \frac{(1 - p')^2}{1 + b_M p'}, \quad (9)$$

where M_{fd} is are elastic moduli (E or G) of the fully dense material, b_M is a porosity dependence constant and p' is fractional porosity. The exponential relation, Eq. (8), proposed by Spriggs [18] and Knudsen [19] has found wide use for fitting modulus–porosity data for ceramics [20]. Although, Eq. (8) is entirely empirical, Rice [20–22] showed that the porosity dependent constant in Eq. (8) is related to the particle stacking and pore shape in the minimum solid area model. The second model, Eq. (9) was developed by Ramakrishnan and Arunachalam [23,24] for determining elastic moduli of porous solids with randomly distributed pores on the basis of the composite spheres model (CSM) [25].

Fig. 3 shows Young's (E) and shear (G) moduli determined by IE as a function of porosity for unreduced (NiO-YSZ) and reduced (Ni-YSZ) anode materials. The modulus–porosity relationships obtained using exponential and CSM models are also shown by separate lines in Fig. 3, while the zero porosity moduli values (E_0 and G_0) and porosity dependent constants (b_E and b_G) are listed in Table 1. The high values of R^2 and small standard errors (Table 1) for both exponential and CSM models indicate that both models provide good fits. The zero-porosity elastic moduli values and porosity dependence coefficients for NiO-YSZ are in relatively good agreement with values reported by Selcuk and Atkinson [11] for 75 mol% NiO-YSZ.

The closeness between the zero-moduli and porosity dependence coefficients determined for unreduced and

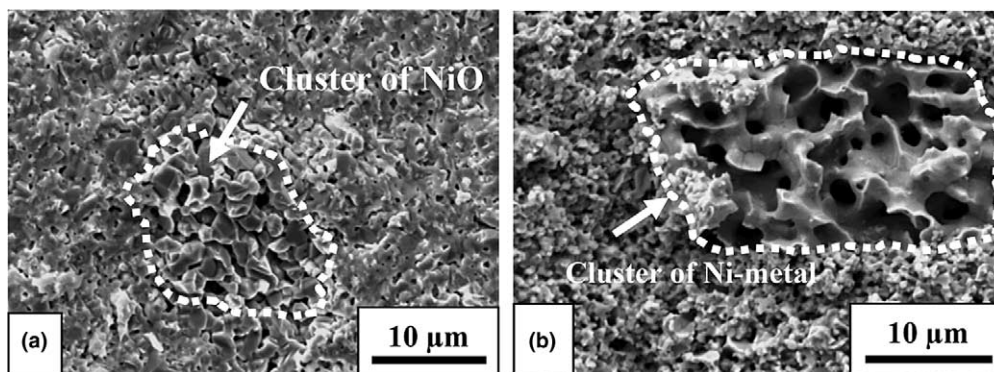


Fig. 2. FESEM micrographs of the fracture surfaces of NiO-YSZ with initial porosity of 6.37 vol% (a) before and (b) after reduction in hydrogen. The marked area on (a) represents a cluster of NiO particles. After reduction such a cluster forms a coarse porous area with interconnecting Ni-metal grains as indicated in (b).

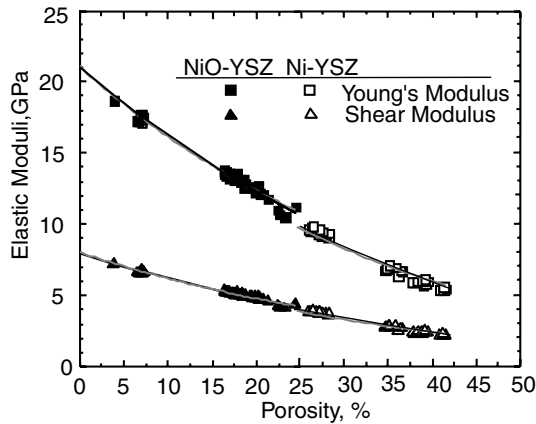


Fig. 3. Young's (E) and shear (G) moduli of unreduced and reduced Ni-based anode as a function of porosity. The results of fitting using exponential and CSM model are represented as gray and black solid lines, respectively.

Table 1

The best fit values of zero-porosity moduli, (E_0 and G_0), the porosity dependence constants (b_E and b_G) and correlation coefficient (R^2) for NiO-YSZ and corresponding Ni-YSZ determined using exponential and CSM models

Model	Material		
		NiO-YSZ	Ni-YSZ
Exponential	E_0 , GPa	210.8 ± 1.4	212.1 ± 1.31
	b_E	2.7 ± 0.04	3.16 ± 0.03
	R^2	0.985	0.995
	G_0 , GPa	80.4 ± 0.5	79.5 ± 0.6
	b_G	2.6 ± 0.04	2.95 ± 0.03
	R^2	0.984	0.992
CSM	E_0 , GPa	209.5 ± 1.4	211.4 ± 0.9
	b_E	0.46 ± 0.05	0.79 ± 0.02
	R^2	0.984	0.998
	G_0 , GPa	79.4 ± 0.6	78.2 ± 0.4
	b_G	0.33 ± 0.05	0.53 ± 0.02
	R^2	0.982	0.997

Average values \pm one standard deviation.

Inside brackets is the 95% confidence interval.

reduced anode material indicates that the decrease of the elastic moduli during the reduction of NiO-YSZ anode is almost exclusively due to increase in porosity [9].

3.3. Biaxial strength

The ambient temperature biaxial strength results for Ni-based anodes were analyzed using a two-parameter Weibull distribution [26] according to:

$$f(\sigma) = 1 - \exp[-(\sigma/\sigma_0)^m], \quad (10)$$

where $f(\sigma)$ is the probability density function of biaxial strengths, σ is the failure stress of a specimen calculated using Eq. (3), σ_0 is the scale parameter or Weibull characteristic strength and m is known as shape parameter or

Weibull modulus.² Weibull distribution parameters were estimated using the maximum likelihood technique and Kaolan–Meier ranking method, while 95% two-sided confidence bounds were calculated using Fisher's matrix method².

Characteristic parameters of Weibull distribution and average strengths for Ni-based anodes with different porosity are listed in Table 2. and are plotted as a function of porosity in Fig. 4. The results in Fig. 4 indicate that the decreases in the characteristic strength with porosity for both, NiO-YSZ and Ni-YSZ specimens can be described by:

$$\sigma = \sigma_0 \exp(-b_\sigma p'), \quad (11)$$

where σ_0 is the strength of the non-porous structure. This relationship was proposed by Ryeshkewitch [26] and Duckworth [27]. However, Rice [22,28] showed that Eq. (11) can be also successfully applied for describing strength–porosity relationship for a wide range of different materials for which the decrease of strength with porosity is proportional to the decrease of elastic moduli with porosity according to the minimum solid area model. The fitting of characteristic strength–porosity data using Eq. (11) results in $\sigma_0 = 158.7 \pm 8.7$ MPa and $b_\sigma = 2.58 \pm 0.34$ with a correlation factor $R^2 = 0.962$ for unreduced anode material, and $\sigma_0 = 473.4 \pm 104.3$ MPa and $b_\sigma = 5.12 \pm 0.67$ with a correlation factor $R^2 = 0.965$. The results shown in Fig. 4 indicate that the characteristic biaxial strength of anode materials decreases after hydrogen reduction. On the other hand, for the same porosity value the characteristic strength of Ni-YSZ anode material is higher than that of NiO-YSZ. Thus, it can be concluded that the observed reduction in biaxial strength after hydrogen reduction is for the most part caused by the increase in porosity in the sample.

In order to analyze the effect of specimen thickness on Weibull characteristic strength, Ni-based anodes with initial porosity of ≈ 22 vol% and different thicknesses (number of laminated layers) were tested in unreduced and fully reduced state. The parameters of the Weibull distributions and average strength values for Ni-based anodes of different thickness are listed in Table 3 while the characteristic strength values are plotted as a function of specimen thickness in Fig. 5. These results show that the characteristic strength and Weibull modulus do not depend on the thickness of NiO-YSZ specimens. Since all examined samples had the same area subjected to in-plane biaxial loading but different thicknesses, it can be concluded that the strength of NiO-YSZ specimens is controlled by surface defects as it was confirmed by fractographic analysis (see below). In the case of Ni-YSZ, the

² The Weibull analysis was carried out using the commercially available software Weibull++¹ (ReliaSoft, Tucson, AZ).

Table 2

Results of biaxial testing at room temperature for four-layers NiO-YSZ and corresponding Ni-YSZ samples after reduction as a function of porosity

	Porosity ^a (vol%)	Biaxial strength ^a (MPa)	Characteristic biaxial strength ^b (MPa)	Weibull modulus ^b	Sample size
NiO-YSZ	6.6 ± 0.8	127.4 ± 17.1	134.6 (125.6,143.6)	8.6 (5.6,12.1)	15
	17.8 ± 0.8	88.9 ± 23.7	97.6 (86.4,110.2)	4.3 (2.9,6.4)	15
	19.8 ± 1.1	86.0 ± 23.7	92.1 (84.5,100.0)	6.8 (4.3,9.8)	15
	21.9 ± 1.8	86.0 ± 21.5	95.4 (83.3,109.1)	4.0 (2.6,6.0)	15
Ni-YSZ	27.4 ± 0.5	107.1 ± 19.7	115.2 (104.2,126.2)	6.1 (3.9,8.67)	15
	36.1 ± 0.4	74.3 ± 10.9	79.1 (73.2,85.4)	7.0 (4.8,10.1)	15
	36.9 ± 1.0	67.9 ± 13.9	73.5 (66.1,81.8)	5.0 (3.5,7.2)	15
	39.8 ± 1.6	50.7 ± 12.0	55.42 (49.2,62.5)	4.5 (3.1,6.5)	15

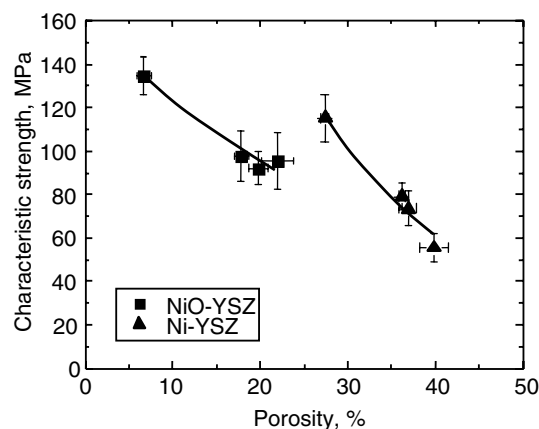
^a (Average value) ± (standard deviation).^b Inside brackets is the 95% confidence interval.

Fig. 4. Characteristic biaxial strength determined from Weibull distribution for four-layers NiO-YSZ and Ni-YSZ samples with different porosity. Solid lines represent results of fitting an exponential relationship to the strength–porosity data. Error bars for strength represent 95% confidence bounds while error bars for porosity represent one standard deviation.

characteristic strength was found to decrease with increasing thickness as illustrated by the results in Fig. 4, while the Weibull modulus was found to increase with the thickness of the samples (Table 3). However, fractographic analysis of Ni-YSZ samples after biaxial testing (see below) could not reveal any differences in the size, type or distribution of the

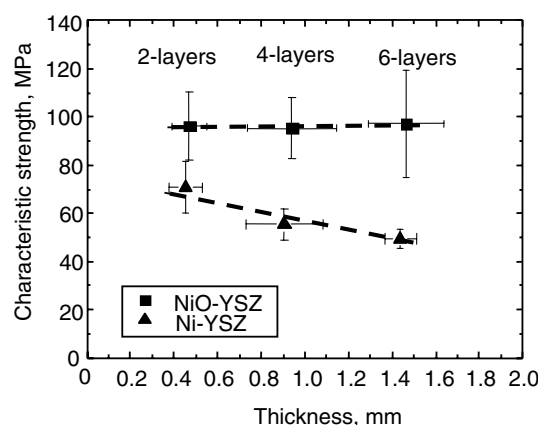


Fig. 5. Characteristic biaxial strength determined from Weibull distribution for NiO-YSZ and Ni-YSZ samples with thickness. Error bars for strength represent 95% confidence bounds while error bars for thickness represent one standard deviation.

strength controlling defects among samples with different thicknesses, because the large amount of porosity makes it difficult to identify the origin of failure. Thus, the reason for the observed decrease in characteristic biaxial strength with specimen thickness still remains elusive at this time.

Fracture surfaces after biaxial testing were analyzed using FESEM. The fracture of Ni-based anode was predominately transgranular before reduction and

Table 3

Results of biaxial testing at room temperature for 22 vol% porous NiO-YSZ and 40 vol% porous Ni-YSZ samples with different number of laminated layers

	# of layers	Thickness ^a (mm)	Porosity ^a (vol%)	Biaxial strength ^a (MPa)	Characteristic biaxial strength ^b (MPa)	Weibull modulus ^b	Sample size
NiO-YSZ	2	0.47 ± 0.08	22.7 ± 1.4	86.5 ± 28.5	96.2 (89.9, 111.5)	3.6 (2.4, 5.4)	15
	4	0.94 ± 0.20	21.9 ± 1.8	86.0 ± 26.4	95.3 (83.3, 109.1)	4.0 (2.6, 6.0)	15
	6	1.46 ± 0.17	21.6 ± 1.0	86.9 ± 34.2	97.2 (77.5, 122.0)	3.2 (1.7, 5.8)	8
Ni-YSZ	2	0.45 ± 0.08	39.3 ± 0.6	63.8 ± 19.7	70.7 (60.6, 81.7)	3.8 (2.4, 5.6)	15
	4	0.91 ± 0.18	39.8 ± 1.6	50.7 ± 12.0	55.4 (49.2, 62.5)	4.5 (3.1, 6.5)	15
	6	1.44 ± 0.07	41.8 ± 1.3	45.8 ± 8.8	49.5 (45.4, 53.7)	6.4 (4.2, 9.6)	15

^a (Average value) ± (standard deviation).^b Inside brackets is the 95% confidence interval.

intergranular after reduction (not shown here) irrespective of the level of porosity. The high level of porosity of the samples usually makes it difficult to identify fracture origins because most of the characteristic fractographic features such as mirror, mist and hackle regions are not apparent on the fracture surface. However, some typical fracture origins in NiO-YSZ and Ni-YSZ samples were identified as illustrated in Fig. 6. These include clusters of NiO particles (Fig. 6(a)), large cavities (Fig. 6(b)), YSZ agglomerates (Fig. 6(c) and (e)) and dimples (Fig. 6(d)) close to the tensile surface in the case of NiO-YSZ specimens. In the case of Ni-YSZ samples, large cavities (Fig. 6(f)), clusters of Ni grains (Fig. 6(g)) and YSZ agglomerates

(not shown here) were usually identified as origins of the fracture.

3.4. Fracture toughness

Average values of fracture toughness, K_{IC} , determined using the double torsion method at ambient temperature are listed in Table 4 and plotted in Fig. 7 for NiO-YSZ and Ni-YSZ specimens with different volume fraction of porosity. It was found that fracture toughness of both, NiO-YSZ and Ni-YSZ decrease with increasing porosity. The results in Fig. 7 also indicate that the reduction process is accompanied by an increase in fracture toughness due to the conversion of NiO into

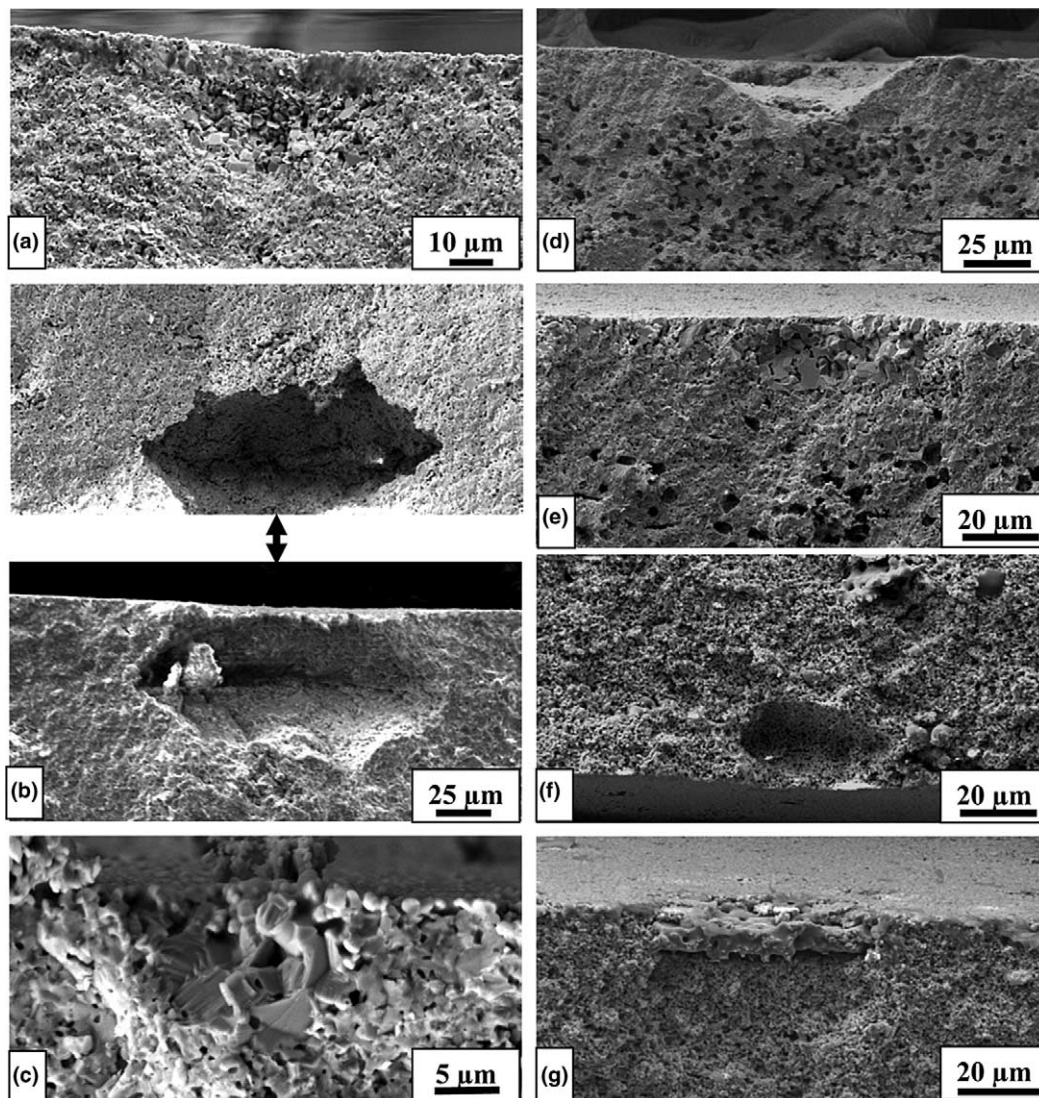


Fig. 6. Typical failure origins: (a) cluster of NiO particles close to tensile surfaces, ≈ 6.6 vol% porous NiO-YSZ; (b) big cavity close to the tensile surface, ≈ 6.6 vol% porous NiO-YSZ; (c) cluster of YSZ grains on the tensile surface, ≈ 6.6 vol% porous NiO-YSZ; (d) surface dimple, 21.9 vol% porous NiO-YSZ; (e) cluster of YSZ grains on the tensile surface, ≈ 21.9 vol% porous NiO-YSZ; (f) large cavity close to tensile surface, ≈ 27.3 vol% porous Ni-YSZ; (g) cluster of Ni grains close to tensile surfaces, ≈ 27.3 vol% porous Ni-YSZ.

Table 4

Fracture toughness of NiO-YSZ and corresponding Ni-YSZ after reduction in hydrogen

NiO-YSZ (before reduction)			Ni-YSZ (after reduction)		
Porosity ^a (vol%)	Fracture toughness K_{IC}^a (MPa)	Sample size	Porosity ^a (vol%)	Fracture toughness K_{IC}^a (MPa)	Sample size
8.8 ± 0.7	1.8 ± 0.4	4	26.7 ± 0.5	3.4 ± 0.2	5
13.5 ± 1.1	2.1 ± 0.2	10	31.8 ± 1.1	3.0 ± 0.1	4
18.8 ± 0.2	1.7 ± 0.1	2	34.4 ± 0.6	2.5 ± 0.1	5
21.8 ± 1.3	1.6 ± 0.2	5	40.1 ± 1.0	2.3 ± 0.5	5
25.3 ± 0.7	1.3 ± 0.1	2	—	—	—
27.6 ± 1.1	1.1 ± 0.1	5	45.9 ± 2.0	1.9 ± 0.2	5

Fracture toughness was determined from double torsion tests.

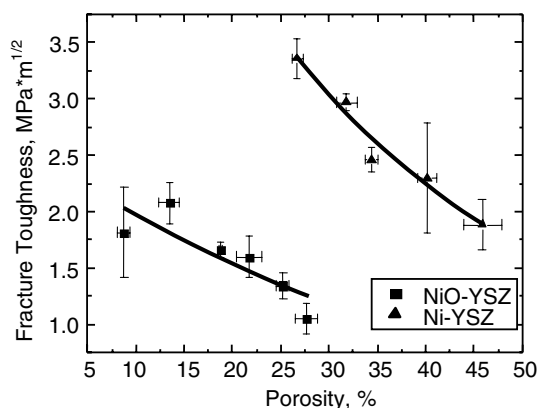
^a (Average value) ± (standard deviation).

Fig. 7. Fracture toughness of NiO-YSZ and Ni-YSZ as a function of porosity. Solid lines represent results of fitting an exponential relationship to fracture toughness–porosity data. Error bars for fracture toughness and porosity represent one standard deviation.

Ni. The results in Fig. 7 can be expressed using following relationship:

$$K_{IC} = K_{IC0} \exp(-b_K p'), \quad (12)$$

where K_{IC0} is fracture toughness of the non-porous structure. The fitting of the model to the results yields values of $K_{IC0} = 2.54 \pm 0.38$ MPa m^{1/2} and $b_K = 2.51 \pm 0.83$ for unreduced anode material and $K_{IC0} = 7.52 \pm 0.93$ and $b_K = 3.03 \pm 0.36$ for reduced material.

Analysis of precracks and fractures surfaces also indicated that the predominant mechanism for crack propagation in NiO-YSZ is transgranular fracture and crack propagates through both, YSZ and NiO particles (not shown here). However, fractographic analysis also revealed the occurrence of plastic deformation of Ni grains in reduced anode materials. Fig. 8 clearly shows a secondary crack on the fracture surface of a double torsion sample in which highly deformed Ni-metal particles bridge the crack surfaces.

3.5. Comparison of porosity–property trends

Relative Young's (E/E_0) and shear (G/G_0) moduli, characteristic strength (σ/σ_0) and fracture toughness

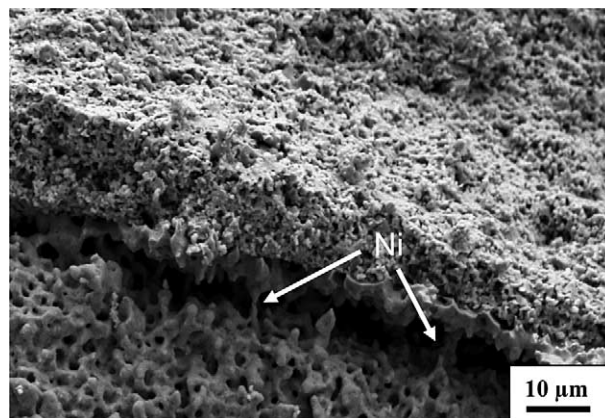


Fig. 8. FESEM micrographs of fracture surface of 26.7 vol% Ni-YSZ of double torsion specimen. Ni-metal bridges are shown in a secondary crack.

(K_{IC}/K_{IC0}) of unreduced and reduced anode samples are plotted in Fig. 9 as a function of porosity. E_0 , G_0 , σ_0 and K_{IC0} are Young's and shear moduli and fracture

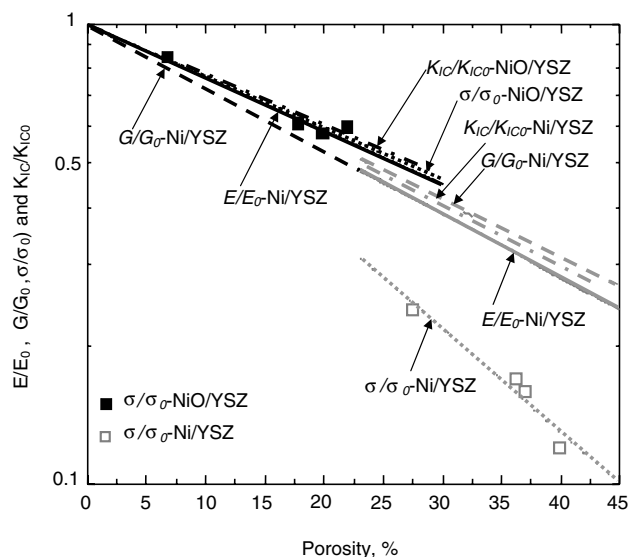


Fig. 9. Relative Young's (E/E_0) and shear (G/G_0) moduli, characteristic strengths (σ/σ_0) and fracture toughness (K_{IC}/K_{IC0}).

toughness of the zero porosity material that were determined using exponential porosity–property relations, Eqs. (8), (11) and (12). The results in Fig. 9 show that the examined mechanical properties, namely elastic moduli and fracture toughness, of unreduced and reduced anode material follow the same porosity–property trend. The porosity dependent coefficient for the elastic moduli and fracture toughness of NiO-YSZ and Ni-YSZ samples is ≈ 3 , which is in good agreement with the predictions of the minimum solid area model for spherical pores in cubic stacking [22,29]. The relative strengths, σ/σ_0 , obtained in this study show different property–porosity trends. Fig. 9 demonstrates that the relative strength of NiO-YSZ follows the same property–porosity trends of the relative moduli and fracture toughness. However, in the case of reduced Ni-YSZ samples, the change of relative strength with porosity differs significantly from the trends for elastic moduli and fracture toughness. In this case the porosity dependent coefficient was found to be ≈ 5 .

As discussed by Rice [22,29], the porosity dependence of elastic moduli, fracture toughness and strength should be similar when strength controlling flaws are larger than the pores. In that case, the porosity dependence of strength is determined by: $K_{IC} = \sqrt{2E\gamma}$ where γ is the fracture surface energy. Since the porosity dependence of γ and E should be similar because theoretically the major determinant of γ is E , fracture toughness has a similar porosity dependence to those of the elastic moduli. However, in the case of crack bridging or interaction of the cracks with the pores, elastic moduli and fracture toughness could have different property–porosity trends. The same property–porosity trends reported here for elastic moduli and fracture toughness suggest that crack-bridging, although observed intensively in Ni-YSZ samples, does not have significant effect on property–porosity trends. The same conclusion may be valid for possible interactions between crack and pores.

On the other hand, according to Griffith's criterion $\sigma_f = K_{IC}/Y\sqrt{c}$ (where σ_f , Y and c are fracture stress, geometrical factor and critical defect size, respectively) the porosity dependence of fracture strength and fracture toughness should be the same for brittle materials, only if the size, type or distribution of the critical defects do not depend on porosity. That is exactly the case for NiO-YSZ (Fig. 9), since fracture toughness and strength follow the same property–porosity trends. However, in the case of the Ni-YSZ samples, σ/σ_0 and K_{IC}/K_{IC0} change differently with porosity for reasons that are not completely clear. At this moment, we can speculate that the presence of the ductile Ni phase that plastically deforms during biaxial testing contributes to the observed differences in property–porosity trends. On the other hand, possible changes in type, size and distribution of critical defects with porosity in Ni-YSZ samples could also be considered as a potential reason for the

different dependence of σ/σ_0 and K_{IC}/K_{IC0} with porosity.

4. Summary

Porosity was found to have a significant effect on Young's and shear moduli, in-plane equibiaxial strength and fracture toughness of Ni-based anodes before and after hydrogen reduction. Young's and shear moduli of both, unreduced (NiO-YSZ) and reduced (Ni-YSZ) anode material were found to decrease with porosity. The decrease in elastic moduli after reduction can be mostly related to the increase in porosity of the samples. The fracture toughness of both, unreduced and reduced Ni-based anodes were also found to decrease with increasing porosity. However, fracture toughness of the anode samples increases after reduction in hydrogen, despite the significant increase in porosity during reduction. Considerable increase of fracture toughness can be explained by formation of the ductile Ni-metal phase during hydrogen reduction. Young's and shear moduli, as well as fracture toughness, have the same property porosity trends that are in good agreement with predictions of the minimum solid area model.

It was also found that the characteristic biaxial strength of Ni-YSZ decreases after the hydrogen reduction due to increase in porosity. However, the strength of the Ni-YSZ with the same porosity as NiO-YSZ is considerably higher because of the presence of ductile Ni-metal phase. In most cases, YSZ agglomerates, the clusters of NiO or Ni grains as well as surface dimples are identified as a strength controlling defects. The relative characteristic strength of NiO-YSZ samples was found to have the same property–porosity trends as relative elastic moduli and relative fracture toughness. However, the relative strength of Ni-YSZ samples decreases with porosity more rapidly than relative elastic moduli and fracture toughness, probably because distribution of critical flaws is also a function of porosity.

Acknowledgements

This research work was sponsored by the US Department of Energy, Office of Fossil Energy, SECA Core Technology Program at ORNL under Contract DE-AC05-00OR22725 with UT-Battelle, LLC. The authors are grateful to their NETL program managers Wayne Surdoyal, Travis Shutz and Donald Collins for their support. The authors are indebted to their ORNL colleagues Beth Armstrong, Claudia Walls, Randy Parten for help with specimen preparation and characterization and to Mr. Tejun Zhen from Drexel University for valuable help with double torsion testing.

References

- [1] Ming NQ, Takahashi T. *Science and technology of the ceramic fuel cells*. Amsterdam: Elsevier; 1995.
- [2] Zhu WZ, Deevi SC. *Mater Sci Eng A* 2003;326:228.
- [3] Atkinson A, Barnett S, Gorte RJ, Irvine JTS, McEvoy AJ, Mogensen M, et al. *Nat Mater* 2004;3:17.
- [4] Morgensen M, Skaarup S. *Solid State Ion* 1996;86–88:1151.
- [5] Lara-Curzio E, Watkins TR, Trejo R, Luttrell CR, Radovic M, Lannutti J, et al. Effect of temperature and H₂-induced reduction on the magnitude of residual stresses in YSZ-NiO/YSZ bi-layers. In: 106th annual meeting and exposition of the American Ceramic Society, Indianapolis, 2004.
- [6] Selcuk A, Atkinson A. *J Eur Ceram Soc* 1997;17:1523.
- [7] Atkinson A, Selcuk A. *Solid State Ion* 2000;134:59.
- [8] Radovic M, Lara-Curzio E, Armstrong B, Walls C. Effect of thickness and porosity on the mechanical properties of planar components for solid oxide fuel cells at ambient and elevated temperatures. In: Kriven WM, Lin HT, editors. 27th Cocoa beach conference on advanced ceramics and composites ceramics. Engineering and Science Proceedings, vol. 24. The American Ceramic Society, 2003.
- [9] Radovic M, Lara-Curzio E. *J Am Ceram Soc*, in press.
- [10] ASTM standard C20.
- [11] ASTM standard C1259.
- [12] ASTM standard C1499.
- [13] Morrell R. *Biaxial flexural strength testing of ceramics materials*, Measurement Good Practice Guide No. 12: National Physical Laboratory, Teddington, UK, 1998.
- [14] Salem J, Powers L. *Guidelines for the Testing of the Plates*. Ibid [8].
- [15] Fuller Jr., ER. An Evaluation of double-torsion testing – analysis. In: Freiman SW, editor. *Fracture mechanics applied to brittle materials*, ASTM Special Technical Publication, No. 678: ASTM, Philadelphia, 1997.
- [16] Pletka BJ, Fuller ER Jr., Koepke BG. An evaluation of double-torsion testing – analysis, *ibid* [15].
- [17] Tait RB, Fry PR, Garrett GG. *Exp Mech* 1987;14–22:14.
- [18] Spriggs RM. *J Am Ceram Soc* 1961;44:628.
- [19] Knudsen FP. *J Am Ceram Soc* 1962;45:94.
- [20] Rice RW. *J Am Ceram Soc* 1993;76:1801.
- [21] Rice RW. *J Mater Sci* 1993;28:2187.
- [22] Rice RW. *J Mater Sci* 1996;31:102.
- [23] Ramakrishnan N, Arunachalam VS. *J Mater Sci* 1990;25:3930.
- [24] Ramakrishnan N, Arunachalam VS. *J Am Ceram Soc* 1993;76:2745.
- [25] Hashin Z. *J Appl Mech* 1962;29:143.
- [26] Weibull W. *J Appl Mech* 1951;18:293.
- [27] Ryshkewitch R. *J Am Ceram Soc* 1953;36:65.
- [28] Duckworth W. *J Amer Ceram Soc* 1953;36:68.
- [29] Rice RW. *J Mater Sci* 1996;31:1509.